Research paper

The stare and chase observation strategy at the Swiss Optical Ground Station and Geodynamics Observatory Zimmerwald: From concept to implementation

Julian Rodriguez-Villamizar [*], Emiliano Cordelli, Thomas Schildknecht

Astronomical Institute of the University of Bern, Sidlerstrasse 5, CH-3012 Bern, Switzerland

ABSTRACT

A sustainable use of the outer space becomes imperative for preserving current operational missions and enabling the placement of new space-based technology in the outer space safely. The uncontrolled growing number of resident space objects (RSO) increases the likelihood of close conjunctions and therefore collisions that will populate the space environment even more. To prevent such situations, orbit catalogues of RSO are built and maintained, which are used to assess the collision risk between RSO. In order to keep the catalogues up-to-date, a worldwide ground-based infrastructure is used to collect observations coming from different observation techniques.

The current study focuses on the so-called stare and chase observation strategy using an active and passive-optical system. The final aim is to correct the pointing of the telescope so that the target will be within the field of view of the laser beam, thus enabling the acquisition of laser ranges. By doing so, objects with poor ephemerides, available e.g. from Two Line Elements (TLE), will not pose a problem anymore for the rather small field of view of the laser beam. The system gathers both angular and range measurements, which can be used for an immediate orbit determination, or improvement, that will enhance the accuracy of the predictions helping other stations to acquire the target faster and permitting the station to repeat the procedure once more.

The development of the observation strategy is particularized for the Zimmerwald Laser and Astrometry Telescope (ZIMLAT), located at the Swiss Optical Ground Station and Geodynamics Observatory Zimmerwald (SwissOGS), Switzerland. Likewise, all the implemented algorithms were tested using real measurements from ZIMLAT and the tracking camera.

1. Introduction: the state of the art

Current observing systems within the framework of Space Situational Awareness (SSA) include the use of radars, passive-optical telescopes and active-optical, i.e. lasers, for tracking, cataloguing and characterization of space debris. If compared against radar or passive-optical systems, lasers have the advantage that their observable, the range, is extremely precise (centimetre level for normal points as shown in the last global International Laser Ranging Service (ILRS) report card [1]). On the other hand, there are important limitations such as the dependency on weather conditions, energy of emitted pulses (particularly important for the so-called non-cooperative targets, i.e. targets without retroreflectors) and of utmost importance: the rather small field of view. The last one prevents the tracking of objects with poor ephemerides, which is a problem rarely found when ranging active targets from the ILRS catalogue [1]. To overcome such limitation, we

designed and implemented the stare and chase observation strategy particularized for the Zimmerwald Laser and Astrometry Telescope (ZIMLAT). The applicability of the implemented observation mode is critical when a close conjunction is foreseen and its uncertainty needs to be reduced. Furthermore, the main difference from the traditional observation strategies, employed in traditional laser ranging observation strategies, comes either from the retrieval of angular measurements without classical astrometric reduction or from the improved quality of angular measurements, which are usually provided by the coarse position of the pointing of the telescope.

The name of the stare and chase was coined after the merge of two well-known observation strategies used in passive-optical systems namely survey and follow-up. Since the novel technique emerged from only passive observation techniques, its evolution up to now will be

---

* Corresponding author.
E-mail address: julian.rodriguez@aiub.unibe.ch (J. Rodriguez-Villamizar).

developed and contextualized by the use of active-optical systems for the observation of space debris.

The first manual implementation of the stare and chase procedure, within the space debris community, dates back to the 4th of September 1992 [2]. The operator was screening acquired frames for glints of objects and then chased the object employing an acceleration joystick. Once the target was close to the boresight, the remaining tracking was done via a video tracker. In one of the successful cases, after five minutes of metric data acquisition, all data was processed and an initial orbit determination (IOD) was performed. About 100 min later, the object was reacquired with 46 s of time bias [2].

The first successful laser ranging experiments to space debris were conducted within 2001/2002 led by Electro Optic Systems (EOS), which operates an observatory located in Mount Stromlo, Australia [3]. The RazorView project was a dedicated programme to demonstrate an operational capability for tracking small space debris objects using laser raging techniques [4]. The experiments demonstrated capabilities for tracking 15 cm objects at altitudes between 1100 and 1250 km. The stare and chase procedure corresponds to their denominated Target Acquisition System (TAS) and Beam Locking System (BLS). The TAS consists of an f/0.75 wide-field telescope equipped with a Charged-Couple Device (CCD) sensor. Its task is to detect the target and to centre it within the BLS field of view. The BLS is a CCD sensor located at the end of the Coudé path of a 1.8 m telescope. Upon initial acquisition, the TAS has control of the telescope tracking servo system, until the target appears in the BLS field of view. Afterwards, the TAS hands-off to the BLS for fine guiding and beam locking [4].

The next attempt to implement and validate a stare and chase observation mode, this time using only passive-optical systems, was done during an observation campaign in the year 2005 [5]. The collaboration between the University of Michigan and the National Aeronautics and Space Administration (NASA) developed a method in which resident space objects orbiting the geostationary ring could be observed and followed for future passes. The discovery of the object was done using the 0.6/0.9 m Michigan Orbital Debris Survey Telescope (MODEST). For the survey and detection, the telescope is initialized and tracks stars moving at fixed lengths in right ascension and declination close to the anti-solar point and avoiding the Earth's shadow. Using a Time Delay Integration strategy, while the object is within the field of view, images are stored. A minimum number of four detections are needed to go to the next step: orbit computation. The correlation of the object per image is done manually by visual inspection and astrometric reduction takes place while the images are acquired. If a minimum number of 4 detections are successful, a circular orbit is estimated and ephemerides are sent directly to the NASA Orbital Debris Program Office at Johnson Space Center in Houston, Texas, where a chaser telescope uses the recently computed ephemeris to reacquire the target [5].

The next study conducted in October 2016 was reported in [6]. Their study focuses on a comparison during the staring mode of the stare and chase observation strategy between two optical-passive sensors: a scientific Complementary Metal–Oxide–Semiconductor (CMOS) and a CCD [6]. Compared to the initial algorithm proposed in [5] the stare, or survey mode, commands the staring camera to point into the near zenith direction with an exposure time of about 0.5 s allowing fast-moving objects to leave a trail and therefore to be discriminated from a point-like star field. For those objects which leave a trail, two subsequent images are subtracted and a threshold algorithm filters the background from the source. For objects observed with shorter exposure time, at least three frames are needed in order to minimize potential false positives. Once the object has been detected, the astrometric reduction takes place by an external commercial software. From the detected positions on the image, a straight line is fitted and extrapolated to a given ahead time which will be used by the telescope to reacquire the target. After their study, it becomes clear that the use of different chip technology according to a different observation task must be highlighted and recommended, e.g. the use of CCD sensors for the

detection of fainter objects despite the longer readout times if compared against CMOS. The proposed methodology was developed as a test-bed for its near future use with laser ranging.

In early 2017 the first successful European stare and chase observation strategy, using a laser ranging system, was reported by the space research institute from the Austrian Academy of Science in Graz, Austria [7]. The hardware corresponds to an analogue video camera with an objective with a focal length of 50 mm and f/1.4 piggyback mounted on the 0.5 m Satellite Laser Ranging (SLR) telescope. While the system is in staring mode, the initial pointing of the telescope in azimuth and elevation is transformed into right ascension and declination. By doing that, the search space is reduced when performing astrometric reduction. Moreover, the number of stars accounted for during plate solving is of the 50 brightest. The plate-solving algorithm takes about 0.2 to 0.5 s and is performed every two seconds; the remaining 1.5 s are used for all object identification tasks. Once a target is detected a number of four frames are acquired to ensure object identification. In order to remove the stars from the background, a relative movement of one pixel between subsequent images is set as a threshold for the removal of the stars. At the same time, the effect of noisy pixels is mitigated by setting a lower bound to the relative movement between successive frames of 15 pixels. The target of interest should move in the range of 1 to 15 pixels between subsequent frames. Once the detection is performed, the retrieved angular data is used to estimate an initial orbit, which is propagated and transformed into the Earth-Centred–Earth-Fixed reference frame, establishing a set of coordinates that will be used by the SLR system to fire laser pulses to the object of interest.

Besides an initial orbit determination, there is the option of active tracking, i.e. a correction of the pointing of the telescope using all measurements available during the object recognition phase. One implementation of such approach was presented in [8]. In the publication, the stare and chase procedure is modularized into three fully parallelized main segments. The first one is the image acquisition; the Georgia-Tech Space Object Research Telescope (0.5 m f/8) points towards the ephemerides given by an initial orbit calculated from a Two Line Element (TLE) set with a finder scope aiding the telescope in the localization of the target. The second segment is the image processing, which uses an enhanced thresholding method. The subsequent data reduction was done via the external tool Astrometry.net [8]. The last segment performs controlling and commanding tasks; the tracking takes as input all differential corrections derived from the object recognition and performs active tracking utilizing a Kalman filter updating the differential corrections with respect to the original orbit given by the TLE. The three modules work together within a closed-feedback loop which proved to work successfully for the case study of the low-Earth-orbit (LEO) target Iridium 914 [8]. Despite the use of a specific tracking module, the committed error is in the order of arcminutes, which proved enough for their application (only-passive) but it is not if the object is planned to be ranged with a laser system.

The previous analysis of the state-of-the-art was needed in order to define the context of the current work, thus highlighting the scientific novelties presented by our research. Specifically, we will present a comparison of methods for the real-time object recognition. We will investigate the advantages and disadvantages of using active tracking instead of an initial orbit determination, and we will guide the reader through the implementation of the selected methods in our operational environment at the Swiss Optical Ground Station and Geodynamics Observatory Zimmerwald (SwissOGS). The latter includes a validation of the measurements acquired by our tracking camera. All the previous work was needed to achieve the final aim of correcting the pointing of the telescope so that the target will be within the field of view of the laser beam, thus enabling the acquisition of laser ranges.

2. Instrumentation and methodology

In this section, we describe the used hardware and the validation of the measurements acquired by the tracking camera. Moreover, we depict the followed methodology for the implementation of the stare and chase as an object recognition and tracking procedure.

2.1. Hardware

Our system consists of the Zimmerwald Laser and Astrometric Telescope (ZIMLAT), with one-metre aperture, a Ritchey–Crétien design and an azimuth-elevation mount. It has a Coudé path for the laser beam and a Nasmyth platform hosting 4 possible focusing positions with focal lengths of 1.2 m, 2 × 4 m and 8 m. Three of them are currently equipped with the Neo scientific CMOS tracking camera, the Spectral Instruments 1100 with a CCD sensor and a single photon counter. The tracking camera is the Andor 5.5 Neo Scientific-CMOS [9] which main characteristics are one electron read noise, a cooling temperature of −40 °C, a 5.5 Mpix sensor (6.5 μm/pixel), an electronic shutter with two possible modes, global or rolling, at different frequencies, easily adjustable through the Software Development Kit. It is mounted using the 8 m focal length position in the derotator platform, which gives an approximate field of view of 9 arcminutes. The pixel scale of the tracking camera is 0.173 arcseconds/pixel. The latter, as the correct orientation matrix of the camera reference system, with respect to the horizon reference system, was derived by plate-solving a series of images containing star fields at different azimuth and elevation positions. The system lens is equipped with filters that block incoming radiation below 500 nm and at 532 ± 5.3 nm. Those filters are used to mitigate the effect of sky background and stray light coming from the backscattered photons from our laser. The timestamp is acquired from a PC-card with IRIG-B signal derived from a GPS receiver at the time of request of the angular encoder values.

2.2. Validation of measurements

Besides the use of angular measurements derived from the tracking camera to correct the pointing of the telescope, all angular observations may be utilized for orbit determination or improvement. An earlier study [10] showed the usability of the measurements collected by the tracking camera for orbit determination. To better understand the outcome from the orbit determination, a comparison against precise ephemerides was conducted. The comparison of the observations collected by the tracking camera, against their interpolated values from precise ephemerides, displayed an error between 15–20 arcseconds [10]. Since the magnitude of the error was 3 times higher than the root-mean-square of the estimated mount model error for ZIMLAT, we decided to inspect the acquisition chain in order to improve the accuracy. We were able to pinpoint issues in the timestamp of the measurements and on the estimation of the laser beam position in the camera reference system.

The timestamp issue was solved by taking the time when requesting the encoder value from the Programmable Multi-Axis Controller (PMAC). Before, the timestamp was derived from the control PC clock which has a time offset of few milliseconds with respect to the actual readout of the angular encoder of the telescope.

In order to solve the second issue, the orientation of the camera reference system was studied. In contrast to the popular plate solving approach, the orientation of our camera reference system is given directly by the pointing of the telescope [10]. In order to find the pointing of the telescope in the camera reference system, a night-calibration session is conducted where only images are stored if there were successful returns from targets ranged by our laser system. For this particular setup, we chose regular targets with accurate predictions from the active catalogue of the ILRS [1]. While we were successfully ranging the target, images were acquired and a pointing position was derived per image in the camera reference system X_i, Y_i. We define the reference point X_{ref}, Y_{ref} as the average of all previously derived pointing positions within the calibration session [10]. In order to transform from the camera into the horizontal reference system, we use the following transformation:

$$\begin{bmatrix} \Delta Az_{app} \\ \Delta El_{app} \end{bmatrix} = \begin{bmatrix} sin\beta & -cos\beta \\ cos\beta & sin\beta \end{bmatrix} \begin{bmatrix} (X_i - X_{ref}) * PixScale \\ (Y_i - Y_{ref}) * Pixscale \end{bmatrix} \tag{1}$$

Note that $PixScale$ is the pixel scale of our sensor (0.173 arcseconds/pixel). The rotation matrix that relates both sets of coordinate systems depends on β which is defined as:

$$\beta = Elevation - DerotatorPos, \tag{2}$$

where $Elevation$ is the elevation of target and $DerotatorPos$ is the position of the derotator, with respect to the elevation axis, both at acquisition time.

The left plots in Fig. 1 show the differences of each pointing position with respect to the reference point in the horizontal coordinate system. An enhancement of the estimation of the reference point includes the modelling of the computed differences. The horizontal and vertical components of the computed differences are each periodic functions ($f(.)$) of azimuth (Az) and elevation (El), as such, admit representation via the two-dimensional Fourier series expansion which can be written as [11]:

$$f(Az, El) = \sum_{i=0}^{\infty} \sum_{j=0}^{\infty} (a_{i,j} sin(jAz)sin(iEl) + b_{i,j} cos(jAz)sin(iEl) + \\ c_{i,j} sin(jAz)cos(iEl) + d_{i,j} cos(jAz)cos(iEl)). \tag{3}$$

Particularizing Eq. (3) with a given degree and order, the coefficients $a_{i,j}$, $b_{i,j}$, $c_{i,j}$ and $d_{i,j}$, are estimated via a regular linear least-squares adjustment. Once the coefficients are estimated, the model is computed for the hemispherical domain in azimuth [0°, 360°] and elevation [20°, 90°]. Note that we consider an elevation mask of 20° and account for avoiding the pointing in the zenith direction. The representation of the estimated model using a degree and order equal to 3 is shown in the right plots in Fig. 1.

The root-mean-square of the estimated coefficients is of 3 arcseconds — both in azimuth and elevation. From the estimated models we can also see that certain patterns suggest a lack of isotropic theoretical behaviour. A potential reason may be the fact that the estimation of the mount model used for regular SLR observations considers the Coudé path, while the tracking camera is mounted on the Nasmyth platform. The conclusion for this section is that we were able to improve the estimation of the reference point using the two-dimensional Fourier series expansion. That correction proved to be crucial for the improvement of the accuracy of our angular measurements.

For the validation of the tracking camera measurements, we chose the Laser Geodynamics Satellite (LAGEOS) -1 which is a regular geodetic target of the ILRS [12]. The observation session on July 11, 2019, lasted 35 min including a gap used by the laser system for avoiding the zenith direction. The apparent angular measurements, collected by the tracking camera, are reduced into topocentric azimuth and elevation and transformed into topocentric right ascension (α) and declination (δ) (J2000 [13]). The approach used for the current validation is a routine orbit improvement with five days of normal points collected from all ILRS network stations. The a priori orbit was taken from the last TLE available through the Space-Track website [14]. By adding the angular measurements to the ranges from the ILRS in the orbit improvement, it is possible to provide residuals of our angular measurements with respect to the improved orbit — estimated using a single batch weighted-least-squares adjustment. The contribution of our angular measurements is that of 35 min of observations with one observation every 3 s (exposure time), with respect to 5 days of range measurements every 120 s (bin size for normal point formation). The weighting of the observation was that of 50 cm root-mean-square for distances and one arcminute root-mean-square for angular observations. Note that the angular observations were down-weighted to assess their goodness-of-it to an only ranges solution. The weighting for the distances was computed as twice the average of the full-width-at-half-maximum of the pulses emitted by the used stations. The results from the adjustment are shown in Table 1 in the radial, along and cross-track satellite-fixed reference frame for the last epoch of observation.

The high precision is in agreement with the expected one due to the precision of the used measurements (centimetre level for normal points
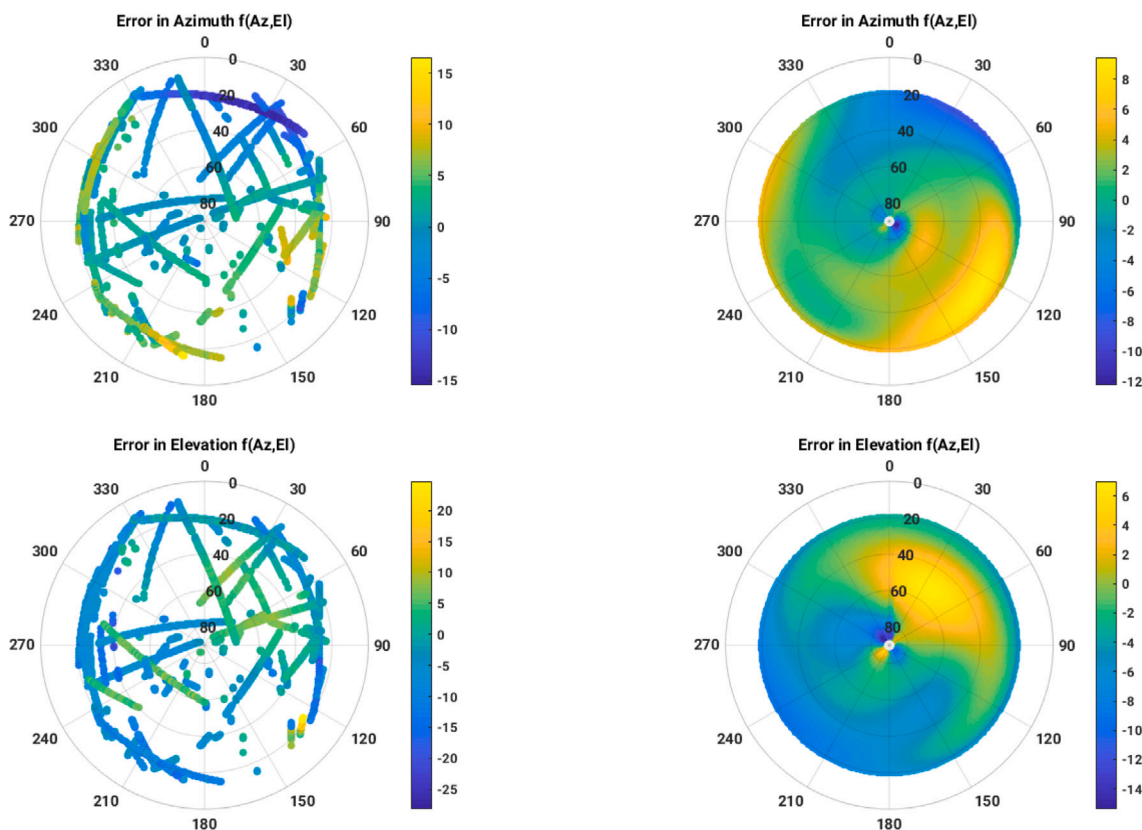
Fig. 1. Left plots: differences of the estimated pointing position per image with respect to the reference point in azimuth (top) and elevation (bottom) as a function of observed azimuth and elevation. Right plots: modelled error of the reference point in azimuth (top) and elevation (bottom) as a function of observed azimuth and elevation. Units of colorbars: arcseconds.
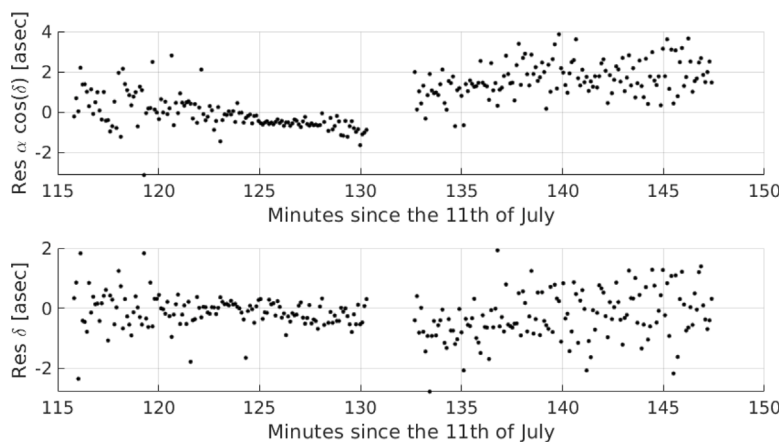

Fig. 2. Angular residuals in arcseconds after orbit determination.

as shown in the last global ILRS report card [1]), the observed arc (≈5 days), and the different portions of the orbit observed by the different tracking stations of the ILRS network. Fig. 2 shows the residuals for the collected angular observations after the orbit improvement.

The root-mean-square for both right ascension and declination is of one arcsecond. The gap in the middle of Fig. 2 is due to the telescope avoiding the zenith direction. The fact that the residuals are not evenly distributed along a zero mean might be due to a time bias, a systematic error in the measurements or due to an orbit modelling deficiency, e.g. we did not estimate scaling factors for the solar radiation pressure. Only the six classical Keplerian elements were estimated, to avoid the absorption of any systematics by the inclusion of dynamical orbital parameters. The symmetry of the trend may be explained by the geometry

in the horizon coordinate system: if the pointing is behind the true position of the target before the zenith, the difference between observed minus computed will be negative while after crossing the zenith, the difference will be positive. A potential explanation for this systematic error could be addressed to the mapping of station-dependent biases from any of the stations used for the estimation of our improved orbit since, in our solution, we did not estimate range biases per station. The inclusion of additional parameters, besides the six classical Keplerian elements in the orbit improvement, could improve the results, however we preferred a minimum parametrization of the problem since we could test for systematic errors directly as we compared directly the collected measurements to precise ephemerides in the form of Consolidated Predicted Format (CPF) [1]. An example of the comparison is shown for
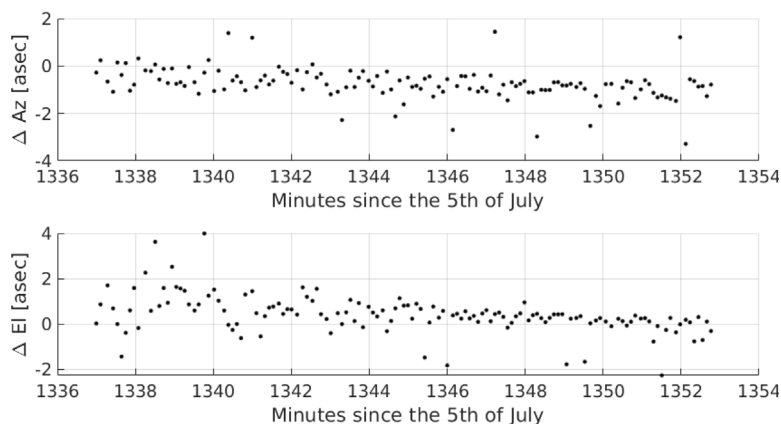
Fig. 3. Differences in azimuth (top) and elevation (bottom) between angular measurements acquired by the tracking camera and interpolated CPF predictions at the observation epoch. Units of differences: arcseconds.

Table 1

Results for the orbit determination of LAGEOS-1 using five days of normal points gathered from the ILRS network plus 35 min of angular observations acquired by the tracking camera. Results are shown in the satellite-fixed reference frame. σ stands for the standard deviation of the estimated component at a 68% of confidence for a normally distributed data set.

Component	Magnitude
σ_{Radial} [m]	0.012
σ_{Along} [m]	0.107
σ_{Cross} [m]	0.045
$\sigma_{V_{Radial}}$ [m/s]	0.001
$\sigma_{V_{Along}}$ [m/s]	0.00001
$\sigma_{V_{Cross}}$ [m/s]	0.0001

a LAGEOS-1 pass on July 5, 2019. The differences between reduced raw observations and interpolated angular values from the CPF ephemeris are shown in Fig. 3. The root-mean-square for both azimuth and elevation is of one arcsecond, and the subtle trend may be explained by the tracking of the controller of the telescope. Furthermore, this cross-validation was also conducted with Cryosat −2, Jason-3 and Lares, all Low Earth Orbit (LEO) satellites. Finally, after the assessment of the order of magnitude of the errors coming from an orbit determination, and a comparison with accurate ephemerides, we conclude that the measurement accuracy has been significantly improved with respect to the first results shown in [10]. In addition to the validation of the measurements, the implemented pipeline is ready to exploit the benefits of including angular measurements, coming from the tracking camera, in the orbit improvement of space debris.

2.3. Methodology

So far we have described the instruments that will provide the observables for the stare and chase observation strategy. The quality of the measurements was tested and validated. In this subsection we will analyse the main modules of the stare and chase observation strategy. To do so, in Fig. 4 we show a general schematic of the complete observation strategy.

The first step, in the stare and chase observation strategy, is to observe in a given direction either fixing an absolute pointing as done e.g. in [6] and [7], or by using an a priori orbit as done in [8]. We opt for the latter since we have specialized telescopes for discovering new objects; therefore, in our case, existing ephemerides are used for initializing the staring mode. Once the object is within the field of view of our staring device, we acquire a series of images. The series of images are processed in real time with the final aim of detecting the object. Object detection is done mainly by thresholding [6,7]. Even

though in [8] several algorithms were tested, there is no in-depth quantitative study of the different methods for an accurate real-time application. The stringent tolerance is given by the rather small field of view of the laser beam, which is between 20–30 arcseconds. In general, it seems that a robust algorithm is needed in order to minimize the false detection provided by thresholding algorithms. In Section 3 we will analyse 3 different object recognition methods highlighting performance and computational time. Additionally, almost all cases reviewed in the state-of-the-art part use an external engine to do plate solving in order to derive astrometric positions from the acquired images. Plate solving is a relatively computational expensive step for a real-time tracking system. In Section 2.2 we proved that we are able to obtain angular errors in the order of one arcsecond (root-mean-square) by using only the pointing of the telescope, thus proving the capabilities for acquiring angular measurements without astrometric reduction.

Depending on the tracking strategy, a threshold for a minimum number of detections (n) becomes imperative, e.g. in [5] a minimum number of 4 detections is needed to compute an initial circular orbit. Systems observing in a fixed direction are limited to collect enough observations while the object crosses the field of view of the staring device; this dependency might be critical for staring devices with a small field of view aiming at fast-moving targets. After n successful detections, the chasing phase of the strategy begins. There are two possibilities regarding the tracking, either the use of new ephemerides after an initial orbit determination [5,7], or active tracking [6,8]. In Section 4 we will compare the two of them selecting the most appropriate one for our system.

Once the tracking starts, we continuously check that the target is within the field of view of the staring device. When the target is within the field of view of the laser beam and the committed radial error is smaller than the 1 km tolerance of our system (Tol), we can collect ranges and angular measurements. The tolerance in the radial error is used for defining the maximum width of the range gate when using laser ranging measurements. Relaxed tolerances will potentially prevent the identification of returns coming from the target since those could be embedded in photoelectron noise. In case we do not comply with the defined tolerance, we can collect only angular measurements. After the setting of the object, all collected measurements will be used for an orbit improvement. The estimated orbital elements will be propagated and possibly disseminated through standard prediction files, e.g. CPF, to other observatories as done in [2,5].

After the selection of suitable algorithms for object detection and tracking, we will analyse their performance in a real-time system. In Section 5 we show how the selected choices can be optimized to achieve high computational performance while complying with the demanding tolerance posed by the small field of view of the laser beam. Finally,
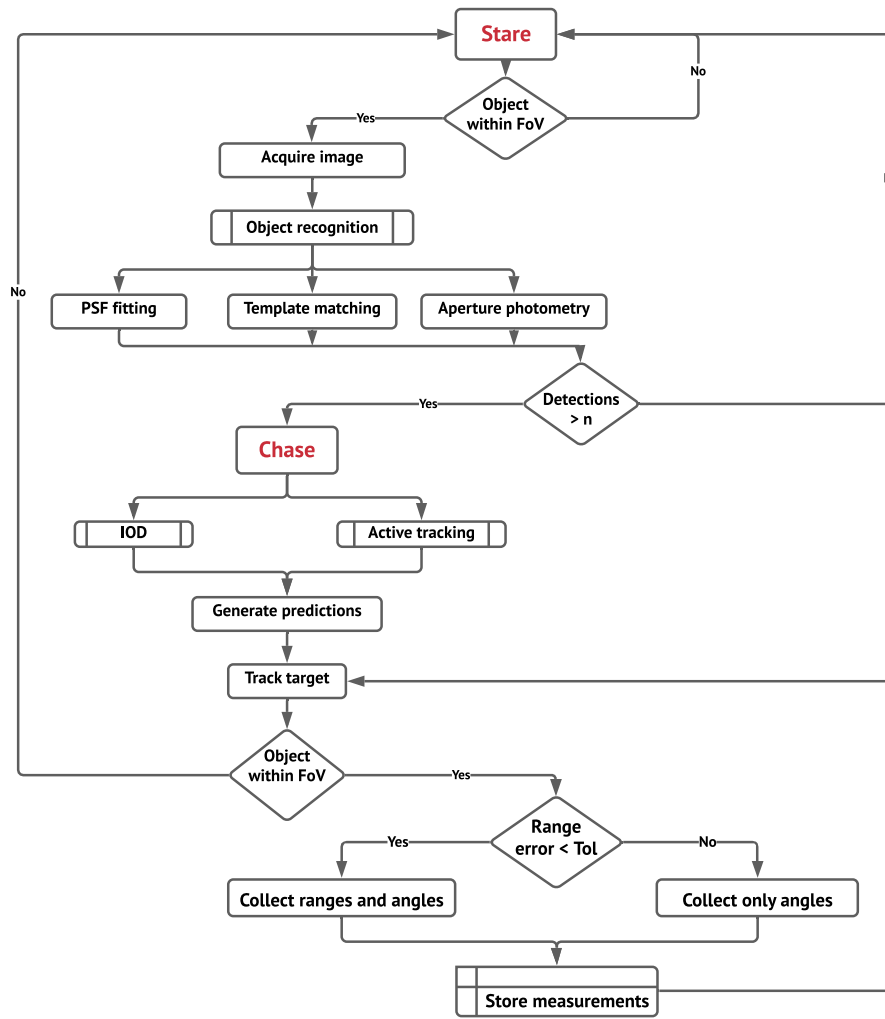
Fig. 4. Flowchart of the stare and chase observation strategy. PSF: point spread function. IOD: initial orbit determination. FoV: field of view.

in Section 6 we evince one of our successful case studies for the decommissioned Environmental Satellite (ENVISAT) when we were able to acquire simultaneously: the apparent changes in brightness, angular and range measurements. Note that the apparent changes in brightness is a by-product of the selected algorithm for object recognition.

3. Object recognition

The automatic detection of sources in astronomical images can be formulated under different approaches. Two widely used are threshold methods based on simple hypothesis binary tests [6,7], and template matching, which correlates a known template against newly acquired images [8]. To further characterize the source, the detected signal is used to derive information about the location of the object on the image, the so-called centroid, as well as the shape, intensity, orientation and other information of the object image. Available methods for centroiding include the weighted average of the coordinates of pixels belonging to the source using their intensity as weight [15], the fitting of a defined point spread function [16] and locating the coordinates of the pixel with maximum cross-correlation between acquired image and template [17]. Note that the fitting of a point spread function could be used as a detection method if prior information about its characteristics is available. In this section, we will focus on the selection of an optimal algorithm that will allow us to perform a real-time object recognition operation minimizing the computational time.

Previous studies for source detection in astronomical images, for non-real-time applications, can be found in [18–20]. Our study compares three different approaches highlighting disadvantages and benefits.

3.1. Fitting of a point spread function

The point spread function (PSF), assuming a perfect imaging system, is the diffraction pattern, in three dimensions, of light emitted from an infinitely small astronomical object and transmitted to the image plane through an aperture objective. A fraction of the light emitted by the source object is collected by the objective focusing it at a corresponding point in the image plane. When the incoming waveform converge and interfere at the focal point, it yields a diffraction pattern of concentric rings of light surrounding a central, bright disk, when viewed in the image plane. The radius of the disk, so-called Airy disk, might be determined by the aperture of the telescope [16]. The image of the diffraction pattern can be modelled by a certain distribution of intensity, e.g. Gaussian, Lorentz or Moffat [16]. In addition to the Airy-disk, the effect of the light transmitted through the atmosphere is quantified by the on-site seeing, which also affects the focusing of the object in the image plane. We model the distribution of intensity of our object image as the following point spread function:

$$I(X, Y) = Zo + A \exp(-a(X - Xc)^2 + 2b(X - Xc)(Y - Yc) + c(Y - Yc)^2), \quad (4)$$

where $a = \frac{cos^2\theta}{2\sigma_x^2} + \frac{sin^2\theta}{2\sigma_y^2}$, $b = -\frac{sin2\theta}{4\sigma_x^2} + \frac{sin2\theta}{4\sigma_y^2}$, $c = \frac{sin^2\theta}{2\sigma_x^2} + \frac{cos^2\theta}{2\sigma_y^2}$, θ is the orientation of the object image in the image plane, Zo is the

Table 2
Estimated Gaussian point spread function parameters. Units of estimated values and their corresponding precision are given by the unit of the parameter (first column).

Parameter	Estimated value	Precision (1σ)
$\theta[deg]$	163	± 0.83
$Zo[ADU]$	186	± 0.007
$A[ADU]$	48	± 1.8
$Xc[Pix]$	251	± 0.51
$Yc[Pix]$	250	± 0.53
$\sigma_x[Pix]$	19.5	± 0.72
$\sigma_y[Pix]$	20.1	± 0.75

averaged background level, A is the amplitude of distribution, X, Y are the coordinates in pixels in the image reference system, Xc, Yc are the coordinates of the centroid of the distribution in pixels and σ_x, σ_y are the standard deviation of the X and Y components of the distribution in pixels.

The observables y of our model correspond to the intensity value (I) for a given position X, Y in the image plane. The cost function to be minimized reads:

$$C(\boldsymbol{x}) = \|y - A\boldsymbol{x}\|_2^2, \tag{5}$$

where $\boldsymbol{x} = [\delta\theta, \delta Zo, \delta A, \delta Xc, \delta Yc, \delta\sigma_x, \delta\sigma_y]^t$ and $A = \frac{\partial I}{\partial P_i}, P_i = \{\theta, Zo, A, Xc, Yc, \sigma_x, \sigma_y\}$.

Note that the problem is non-linear, therefore Eq. (4) is linearized and differential corrections are estimated per each iteration until reaching convergence. The Levenberg–Marquardt optimization algorithm [21] was implemented in order to avoid convergence towards local minimum. Fig. 5 depicts an example of a space debris object image and its estimated point spread function.

The estimated parameters and precision are shown in Table 2. Note that for those parameters describing the shape of the PSF in pixels, their correspondent angular unit can be computed by multiplying the value with the pixel scale (0.173 arcseconds/pixel).

One advantage of using this method is that it relies on the physical representation of the imaging process on the image plane. The fact that all parameters describing the point spread function can be estimated all at once is desirable since the use of a different method for computing e.g. the background can influence the other sets of parameters. Contrary to the benefits, the algorithm took up to five seconds in order to converge until a rather conservative tolerance of e^{-16}. The explanation for the tolerance is given by the seek of the true computational minimum within the function which is minimized. If the tolerance is relaxed, it is possible that the estimated solution does not satisfy the strict minimization of Eq. (5). Additionally, due to the non-linear nature of the distribution of intensity, the algorithm needs a first guess so that the estimated differential corrections are close enough to the linear term of the Taylor series expansion. An increase in the magnitude of the background due to clouds, trails of stars, etc. might prevent the convergence of the least-squares solution.

3.2. Template matching

The principle of this method is the two-dimensional cross-correlation, which for a discretized spatial domain reads:

$$Corr(x, y) = \sum_{u=-h}^{h} \sum_{v=-h}^{h} I(x + u, y + v)T(u, v), \tag{6}$$

where the resulting pixel in $Corr(x, y)$ is the result of taking the pixel $I(x, y)$ from the image, multiplying it by every single pixel of the template $T(u, v)$, and adding all — in the spatial domain. We define the template $T(u_{0...(2*h)-1}, v_{0...(2*h)-1})$ as a square sub-image, or kernel, of radius h. Afterwards, the pixel coordinates with maximum correlation,

with respect to the template, are the ones estimated for the centroid. Its use for a real-time application was reported in [8], but discarded due to the long processing time. In our case, we were able to code the algorithm with a computational time in the order of 0.01 s per image which is translated into about two arcseconds for a low Earth orbiter object with an apparent angular velocity of 3.11 arcminutes/sec. After an in-depth study of the method, we found that there are three ways in which the computational time of the algorithm can be decreased, e.g. by using the convolution theorem and performing all operations in the frequency domain [22], by using the definition of the separable kernel for the template [22] – possible if we model our template as a 2D-Gaussian kernel – or by transforming the two-dimensional problem into a one-dimensional. Furthermore, the use of a multicore machine will allow us to split the incoming image into the number of cores, perform the algorithm core-wise, and reconstruct the final solution. Further details about its implementation are provided on request since this procedure failed with newly acquired images containing trails of starts or noisy background with random saturated pixels.

3.3. Aperture photometry

This method is widely used for the determination of light curves [15]. The method consists of placing inner and outer concentric circles on the target, for the estimation of the source and background respectively. The estimation of the brightness of the target takes place by summing all pixel counts within the source aperture after the subtraction of the background estimated from the outer ring [15]. If compared against the fitting of a point spread function, we only estimate the parameter A for all pixels inside the inner aperture, i.e. the amplitude of the point spread function. In order to estimate the shape of the distribution defined by σ_x, σ_y, we assume $\sigma_x = \sigma_y$ and that its value is given by the site seeing conditions, which is obtained by taking the full width at half maximum (FWHM) provided by its PSF [23]. We approximate its PSF by computing a profile plot of normalized integrated intensities around concentric circles as a function of the distance from the centroid of the object image. Once we are able to obtain the FWHM, the radius for source and background are obtained by multiplying the distance at FWHM by 1.7 to get the source radius, 1.9 to get the inner-radius of the background ring and 2.55 to get the outer-radius of the background ring [24]. Fig. 6 shows an example of the estimation of radius both for source and background.

In order to find the centroid coordinates X, Y of the object image, a sequence of processing steps is needed. Those steps are implemented in Algorithm 1. Despite the sequence of steps needed in this method, an efficient implementation yields a computational time of 0.005 s per image. It also proved to be more resilient for images containing star trails, clouds and bright background. In Section 5, we will provide more details regarding the optimization of parameters for the presented approach.

Algorithm 1: Estimation of the centroid coordinates of the object image.

Procedure SubFrame // Crop image around the object image into a subframe.
Procedure MedFilt2 // Convolve the subframe against a median filter.
Procedure SubBack // Subtract the estimated background from the convolved image.
Procedure GetCentroid // Estimate the coordinates of the centre of the object image by a weighted average of the non−negative pixels using the intensity of each of them as weight.

It is important to notice that besides detecting the object, we are also able to retrieve evidence of the attitude and attitude motion of the target. The outstanding by-product is a real-time light curve depicting
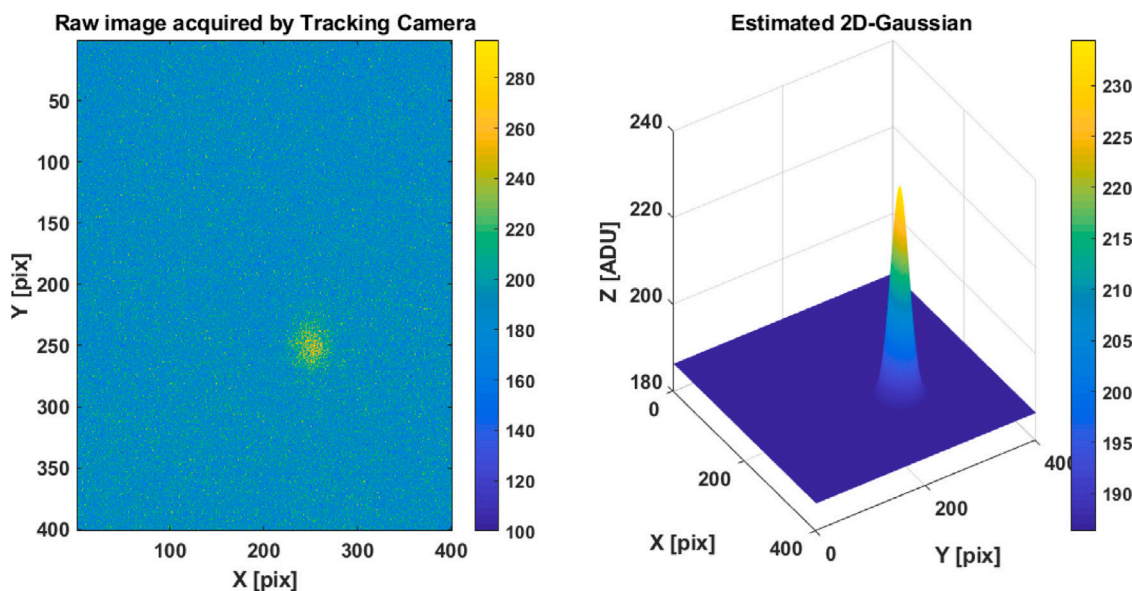
Fig. 5. Case study of fitting a Gaussian point spread function given a raw image acquired by the tracking camera. Units of colorbars: Analogue-To-Digital unit (ADU).
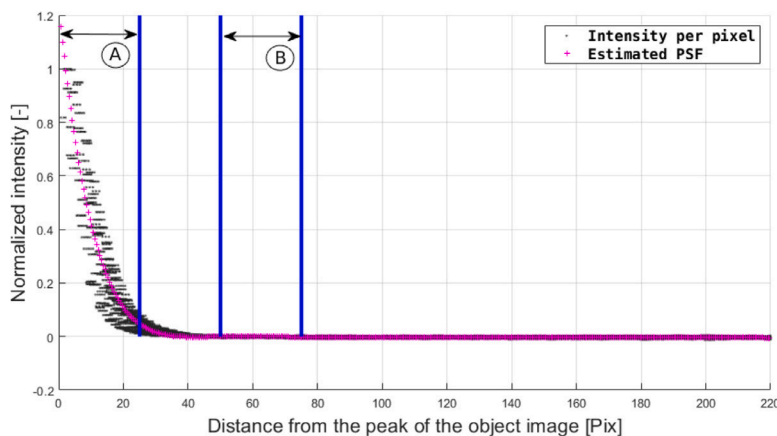

Fig. 6. Radial PSF profile showing normalized intensity values against distance from the peak of the object image. A: radius of the inner aperture. B: radius of the outer aperture.

apparent changes in brightness of the object. The new observable provides another measurement to the original set of azimuth, elevation and range. In addition to the information about the attitude and its evolution with respect to time, the estimated changes in brightness might correspond to specific epochs when the target, despite of being centred in the field of view of the laser beam, was not reflecting back enough photons to distinguish them from the photoelectron noise. Furthermore, the fusion of light curves obtained by ranges and apparent brightness might complement and refine the target attitude information.

3.4. Centroiding and light curve validation

In Section 3.3 we showed that the outcome of the object recognition comprises the coordinates of the object image and its apparent brightness. To validate the results after the full implementation of the procedure in the processing chain, and to set a lower and upper bound to the committed error, we do a comparison against the solution obtained by a non-real-time software: AstroImageJ (AIJ) [24]. The validation compares the real-time estimated centroid and light curve using our implementation against the post-processed centroid and light curve extracted from AIJ. The target used for the current validation is the decommissioned satellite ENVISAT observed on the 17th of October 2019 during daylight.

In Fig. 7 top-left plot, we can see that the object image does not have a homogeneous point-like shape but has a rather spread feature in a nonsymmetrical fashion. Main reasons for this shape might be attributed to a combination of the site seeing with strong turbulence, the astigmatism of the telescope optical assembly and the active tracking. The estimation of the inner and outer rings (top-left plot in Fig. 7) corresponds to the method explained in Section 3.3. The comparison, between our light curve and the one retrieved by AIJ (top-right plot in Fig. 7), shows that both solutions are in agreement. The differences can be explained by the slightly different values in the estimated centroid (bottom plot in Fig. 7), which will not place the annular rings in the exact same location affecting also the estimation of the new apertures and subsequent parameters derived thereof. The comparison of the estimated centroids shows that the solution provided by the object recognition and prediction are the same for the first eight frames due to the construction of the sliding window. The remaining part depicts a rather smooth trajectory with no outliers. The maximum difference is less than 20 pixels which correspond to 4 arcseconds. Given that the tolerance demanded by the SLR system is of about 20 arcseconds, we conclude that the method complies with the system constraints delivering also an extracted real-time light curve.
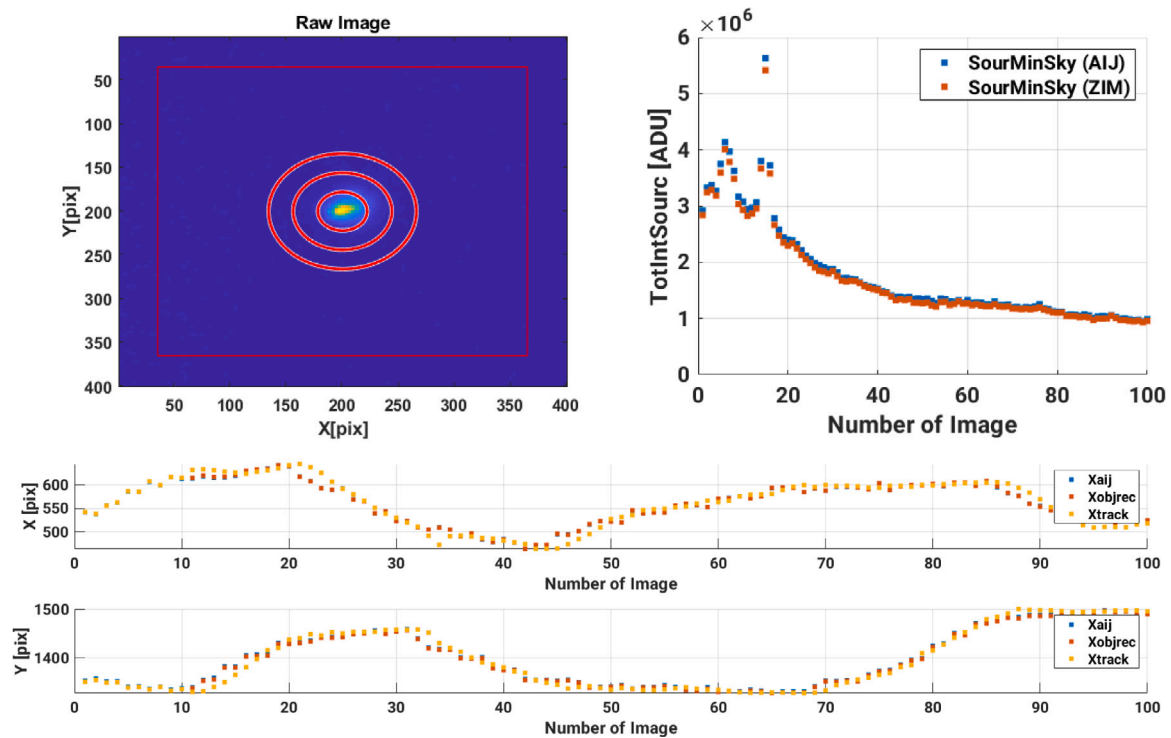
Fig. 7. Validation of the algorithm for centroiding and light curve determination. Top-left: raw image with estimated inner and outer rings. Top-right: comparison of source-minus-background between AIJ and our solution (ZIM). Bottom: comparison between centroid estimates using AIJ (**X**aij), object recognition (**X**objrec) and predicted values (**X**track).

4. Tracking

In the review of the stare and chase observation strategy, we saw that the chasing step of the procedure involves either the use of an initial orbit determination, or active tracking. The use of an initial orbit determination might not be optimal for highly automated systems, since the inclusion of the newly generated ephemerides might not be done within an existing session. Furthermore, one unanswered question addresses the usability of the IOD solution. Specifically, it is not a trivial matter to give a bounded solution to the question: how good is the estimated initial orbit and therefore until when will the target be within the field of view of my chasing device? The number of observations used in an initial orbit determination corresponds to the number which the sensor can collect while the object crosses the field of view of the staring device. Consequently, the number of observations is a function of the apparent velocity of the target, the field of view of the system and the exposure time. In cases with reduced field of view aiming at fast-moving targets, a real-time correction for the pointing of the telescope is preferred, i.e. active tracking. A disadvantage of the active tracking approach, when it relies only on an object-recognition step, is that wrong estimates of the corrections will involve wrong slew movements of the telescope. To prevent an undesired slewing motion, a close-feedback loop is developed guaranteeing a smooth trajectory of the object, which makes use of a sliding window containing the historical record of the coordinates of the target previously determined in the object recognition step. In this section we will study the advantages and disadvantages of using either IOD or active tracking.

4.1. Initial orbit determination

After the computation of an initial orbit using only angular measurements with the method described in [25], its propagation and inclusion within the observation scheduler must be analysed. Ideally, the solution provided by the initial orbit determination should be updated as soon as the target is close to exiting the field of view of the chasing device.

Nevertheless, it might be a more convenient strategy to correct the pointing of the telescope in real time, i.e. active tracking, so that the observed arc is longer and the orbit improvement will be significantly better. In order to support the previous statement, a case study for the Experimental Geodetic Payload (AJISAI) is presented. The target was chosen since there is accurate ephemeris available [12], which will be used to compute formal errors with respect to each of our solutions. Note that for the application of the Stare and Chase observation strategy, i.e. the space debris domain, the ephemerides available through the different analysis centres are considered to be accurate [12]. We took such ephemerides as reference since we were able to track the targets, e.g. AJISAI, using its latest available ephemerides with our laser system, meaning that the ephemerides were good enough to enable the gathering of laser ranges, which is the main aim of the observation strategy. Real observations collected by ZIMLAT and the tracking camera on the 8th of September 2018, corresponding to a high culmination pass, are used for simulating a stare and chase observation scenario. An exposure time of 0.1 s was used through the entire pass. Range measurements in full rate form are available from our laser system using a repetition rate of 100 Hz. Table 3 shows the type, angular (Ang) or ranges (Rg), and the number of observations used in the orbit determination procedure. The target acquisition fields correspond to: the possibility to follow the target until setting (Vis Pass), ranging the target within the same pass (Rg pass), reacquiring the target using the staring device for the subsequent pass (Vis Next) and ranging the target within the subsequent pass (Rg Next). We define the acquisition of the target (Vis) if the total angular error is smaller than the field of view ($\approx$ 9 arcminutes) of our tracking camera. Likewise, we consider acquisition of ranges (Rg) for radial errors smaller than 1 km. The latter is given by the maximum admissible width of the range gate of the laser system.

The first orbit solution (IOD) is estimated using only angular measurements collected while the object was crossing the field of view of the staring device. In addition, the eccentricity and perigee passing time were constrained to zero under a circular orbit assumption. The case IOD in Table 3 shows that with the minimum number of angular

Table 3
Orbit solutions using a different set of observations within different parts of the observed arc. Case study for AJISAI observed the 8th of September by ZIMLAT and tracking camera.

Orbit solutions AJISAI						
	Type Obs.		Target acquisition			
Case	Ang	Rg	Vis pass	Rg pass	Vis next	Rg next
IOD	22	0	No	No	No	No
OI*	82	0	No	No	No	No
OI**	262	0	Yes	Yes	No	No
Ang Mid	292	0	Yes	Yes	No	No
Mer Mid	292	30	Yes	Yes	No	No
Ang Mid-End	322	0	Yes	Yes	No	No
Ang Mid Mer End	322	30	Yes	Yes	No	No
Mer Mid-End	322	60	Yes	Yes	Yes	Yes

observations collected by the tracking camera, while the object with an apparent angular velocity of ≈ 3.11 arcminutes/sec crosses the field of view of the staring device, is not enough for chasing the target. Two more orbit improvements are needed in order to chase the object until it sets. The orbit improvements (OI* and OI**) are performed also assuming a circular orbit. The second orbit improvement is needed since the first one does not allow to follow the target until the end of the pass, making use of the measurements collected until the tolerance is exceeded. Note that after the second orbit improvement (OI**), the improved orbit enables the use of ranges, since the error committed in the range is within the tolerance of the range gate. To reacquire the target, orbits with the classical six Keplerian orbital elements are estimated considering perturbations due to the gravitational potential of the Earth, third body perturbations and the solar radiation pressure acting on the known cross-section of the target. Five different situations are simulated: using only a few angular observations in the middle of the arc (Ang Mid), few angular and ranges in the middle of the arc (Mer Mid), only angular observations in the middle and end of the arc (Ang Mid-End), angular observations in the middle of the arc and merged at the end (Ang Mid - Mer End) and using merged observations in the middle and end of the arc (Mer Mid-End). The latter is the only combination that allows the reacquisition of the object for the next pass. In order to see the evolution of the error with respect to each solution and time, we did a comparison against precise ephemerides in the form of CPF. The total angular error (top plots), besides the range error (bottom plots), are shown in Fig. 8 for the same and subsequent pass. The comparison starts with the solution obtained from the IOD using the measurements available while in staring mode. As soon as the total angular error is greater than the fixed tolerance, we compute an improved orbit using all measurements collected until then (blue dots in Solution for Same Pass plots of Fig. 8). After the first orbit improvement (OI*), we see in the red dots a drastic immediate reduction of the angular error, but soon the angular tolerance is reached and again all observations collected until then are used for another orbit improvement (OI**). The latter solution enables the tracking of the target, and therefore acquisition of angular observations and ranges, until the object sets. Finally after adding different measurements in different portions of the observed arc, the only combination that allows the reacquisition of the target is the one that uses merged observations at the middle and at the end of the arc (green dots Solution for Subsequent Pass plots of Fig. 8).

The main conclusion is clear: the observation of a longer arc spanning the complete pass of the target over the station, besides the possibility to fuse angular observations and laser ranges, will generate an orbit that will allow the reacquisition of the target for subsequent passes. The decision on what for a tracking approach to use relies mostly on the system which runs the SLR observation software. If the inclusion of updated ephemerides can be done within an existing observation session, then the use of an initial orbit determination should be
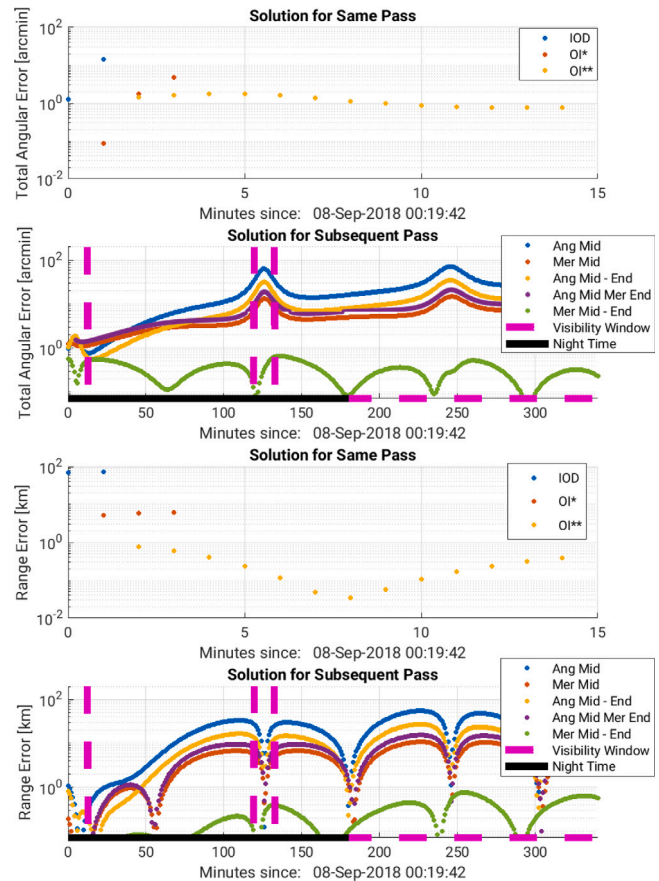
Fig. 8. Comparison of orbit solutions using a different set of observations within different parts of the observed arc against precise ephemerides in form of CPF. The solutions available for the same pass are an initial orbit determination under a circular orbit assumption (IOD), and two subsequent circular orbit improvements (OI* and OI**). The solutions available for the subsequent pass show a full orbit improvement (six Keplerian elements) adding only angular observations in the middle of the arc (Ang Mid), adding merged observations in the middle of the arc (Mer Mid), adding only angular observations at the middle and end of the arc (Ang Mid-End), adding only angular in the middle and merged observations at the end of the arc (Ang Mid Mer End) and finally merged observations in the middle and at the end of the arc (Mer Mid-End).

implemented. On the other hand, for highly automated systems running a session, which will need to abort the current session in order to update the predictions, another approach must be used. A disadvantage of the latter is the need to use an a priori orbit of the object to generate differential corrections to rectify the pointing of the telescope in real time. Nonetheless, such orbit can be retrieved from public catalogues, TLE predictions, or even generated by other telescopes, possibility that we have at the SwissOGS thanks to the variety of telescopes and sensors. Note that if the chasing device is passive-optical and has a wide field of view, the angular tolerances are relaxed and therefore the usability of the solutions depicted in Fig. 8 could be used for a longer time. However, the timing issue related to the uploading of recomputed ephemerides remains critical for fast-moving objects.

4.2. Active tracking

Contrary to an initial orbit determination, an active tracking approach makes use of an existing orbit and improves it using the offsets in azimuth and elevation derived from the object recognition step. In case of wrong detections by the object recognition, the tracking may fail. To prevent such situations a closed-feedback loop is developed. For the design of the closed-feedback loop, we study how these corrections

may look like. To achieve this, we simulate a TLE vs. CPF scenario for AJISAI, which shows the type of corrections that we will most likely encounter in a real-time situation. The TLE acts as the ephemerides that we will have available while the CPF represents the real position of the object in the sky. Fig. 9 shows the differences in the horizon coordinate system (left) and the satellite-station geometry (right).

In Fig. 9 we see that we have two smooth functions that depend on time and orbit (TLE and CPF). The maximum error in azimuth occurs as soon as the target gets closer to the zenith direction. The symmetry of the error in elevation corresponds to the explanation provided in Section 2.2 and is minimum at the time of closest approach with respect to the observing station. We approximate the trajectory by a polynomial of degree n justified by the approximation Stone–Weierstrass theorem [26]. Additionally, the observation equation reads:

$$X_{obs} = X_{true} + \eta_x,$$
$$Y_{obs} = Y_{true} + \eta_y, \tag{7}$$

meaning that the observed position of the object is our measurement for the estimation of the trajectory. The term $\eta_{x,y}$ refers to the noise of the measurements whose probability density function is unknown. Note that the estimation of the probability density function of the noise is not trivial since our observation conditions are different every time that we observe, thus influencing the noise differently. The latter implies that the samples are not independent, identically distributed and ergodic [27]. Despite the fact that the distribution of the measurement noise is unknown, the estimation of the trajectory can be done via a regular least-squares adjustment [28].

Having formulated the dynamical model, i.e. trajectory, and the observation equations, we derive our tracking algorithm as a sequential sliding window method. The algorithm consists of a prediction window based on an autoregressive approach, i.e. estimation of the future state vector based on its past values. The mathematical model reads:

$$X_t = \sum_{i=0}^{Degree} \phi_i (t - to)^i_{t-1} + \varepsilon_{t-1}, \tag{8}$$

where X_T is the coordinate component at time t, ϕ_i are the coefficients to be estimated for predicting the state at time t and ε_{t-1} is the committed error in the estimation of X_T. The estimation of the coefficients is done via a regular linear least-squares using the available $t-1$ observations within the sliding window. Simultaneously to the previous window, we construct an error window based on an autoregressive moving median approach. From a historical records of observations and predictions, we calculate the observed-minus-computed (OmC) term and estimate the median for all entries within the window. The mathematical model reads:

$$\tau_t = MED(\tau_{t-1}), \tag{9}$$

where MED is the median estimator over the window containing OmC values. In order to exclude outliers in the estimation of the updated state of the target, a scoring window marks an observation as a potential outlier if the following condition holds true:

$$SC_t = \begin{cases} 1, & |OmC|_t > \tau_t + 6MAD, \\ 0, & otherwise, \end{cases} \tag{10}$$

where MAD is the median absolute deviation. The factor of six is used as a Ref. [29]; it comes from the relationship between the MAD and the standard deviation, at 99.998% confidence, for normally distributed data sets. All the previous steps are gathered in a set of procedures described in Algorithm 2. It is assumed that there are a minimum number of detections within the sliding window which will initialize all procedures described in Algorithm 2. The inversion of the normal equation system, needed for the estimation of the coefficients of the polynomial of degree n, was performed using the Cholesky factorization algorithm [30].

Algorithm 2: Active tracking based on an autoregressive approach.

Procedure PWLSQ // Predict state of the target using unmarked observations.
Procedure GetNewMeas // Subtract the new observation from the prediction.
Procedure UpdErrorWin // Update the error window and estimate its median.
Procedure MarkObs // Mark observations which exceed the threshold.
Procedure UpMeasWin // Remove marked observations from observation window.

From the implementation of the algorithm, we were able to pinpoint the following dependencies: number of points within the sliding window, degree of the polynomial and the handling of data gaps within the observation session. Fig. 10 shows the tracking solution of the trajectory (shown in Fig. 9) using different data points, within the sliding window, and different polynomial degree. A higher degree than two was found to yield an over-parametrized solution, which led to the modelling of outliers as part of the trajectory in worst-case scenarios.

The number of points available in the sliding window is a function of the exposure time which affects the frame rate, thus critical for long exposures. Assuming a frame acquisition every second, we found that a number of nine data points was enough to keep a fast execution time while keeping the target within the field of view of the laser beam. Further test involving a frame acquisition every 5 s demonstrated to keep the target within the tolerance of 20 arcseconds. Regarding the degree of the polynomial, both linear and quadratic proved to keep the target within the specified tolerance, but as it can be seen in Fig. 10 the quadratic solution yields better accuracy. The critical points of the functions in Fig. 9, after differentiating using a finite-difference scheme, match with those local extrema of the OmC displayed in Fig. 10. It is expected since the difference between the function itself (Fig. 9) and the function used to approximate its future value (a polynomial of degree n), when taken for a such a short interval of time yield the nth derivative. That explains why a higher polynomial degree yields better accuracies, i.e. it adapts better to the function to be approximated reducing the difference with respect to it. The same reasoning explains why a higher number of points in the sliding window yields larger errors. Finally, the data gaps can occur because the telescope might be scheduled to observe other targets (interleaved with the current pass) or it needs to avoid certain pointing directions, e.g. at the zenith, consequently, the algorithm was designed to handle those gaps and reinitialize by itself when the event is detected.

5. Implementation in a real-time system

All algorithms shown in Sections 3 and 4 were implemented in the Matrix Laboratory (MATLAB) software suite [31] avoiding the use of built-in functions to ensure portability. Only selected ones were migrated into Delphi and coded using the Delphi XE2/C++Builder XE2 compiler [32]. The migration into Delphi was driven by the already existing baseline of the software interfacing with the Software Development Kit of the tracking camera. The implementation of the selected algorithms in a real-time system posed several challenges. It had to be flexible, thus regular operators can make use of it without changing parameters within the source code, the execution time must be short and the algorithm for object detection must be accurate in order to lock the target within the field of view of the laser beam. In the previous subsection, we saw that the procedure is accurate when compared to an ultra-precise photometric software suite [24]. Nonetheless, in this section we explore in detail several customizations of the method in order to decrease even more the computational time.
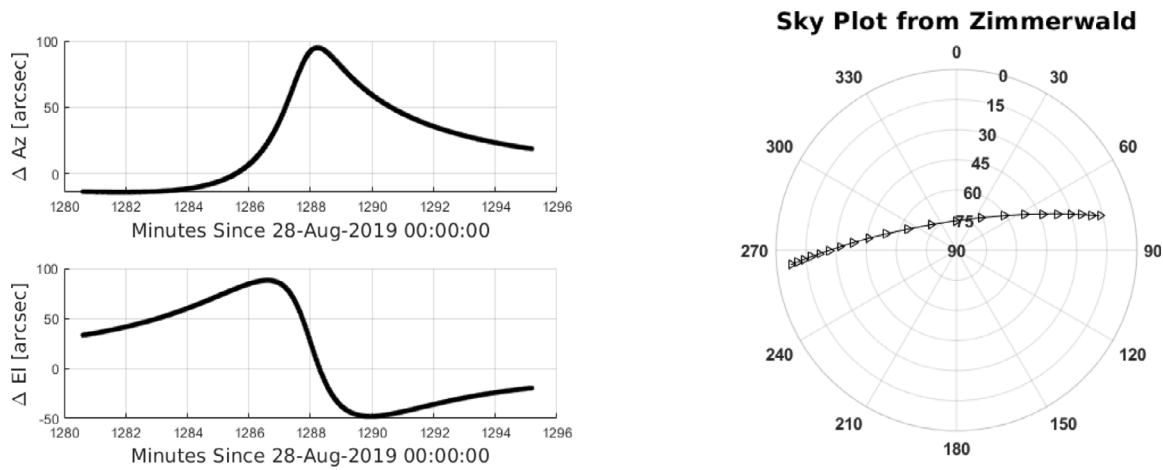
Fig. 9. Differences in the horizon reference system of ephemerides generated by TLE and CPF for AJISAI (left) for a high culmination pass over Zimmerwald (right).
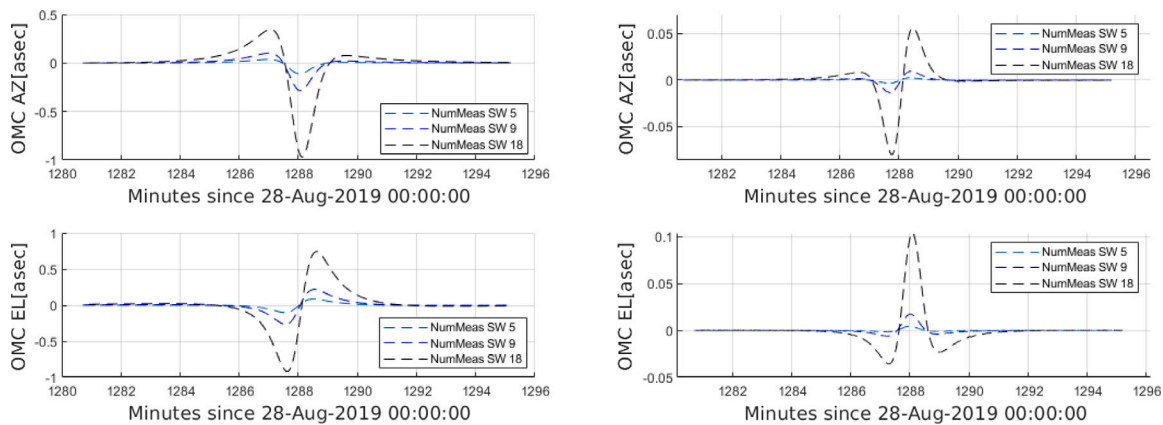

Fig. 10. OmC terms in arcseconds for azimuth (top) and elevation (bottom), using a linear (left) and a quadratic (right) polynomial for the prediction of the coordinates of the target. Each solution depicts the number of measurements within the sliding window (NumMeas SW) that were used for the tracking.

5.1. Optimization of the object recognition procedure

In Section 3.3 we showed that to find the radii for source and background we make use of the cross-section of the object image, in the X and Y axes, and use their respective profiles as an approximation of the PSF, computing finally the different radii for source and background using the FWHM.

The object of interest on the image plane takes only a portion of the full-frame; since the computational load depends on the size of the image, a subframe of the image will yield a faster execution. We decided to specify a subframe of 400×400 pixels, which will give a diagonal of approximately 1.6 arcminutes. It will take about half a second, for an object with an apparent angular velocity of 3.11 arcmin/sec, to cross that diagonal. The algorithm proved to run at the millisecond level, thus being able to correct the pointing of the telescope with enough margin.

The next procedure that was optimized was the selection of a suitable kernel and step size for the convolution of the subframe against the median filter. The criteria used for the selection of the kernel and step size of the median filter are the minimization of wrong pixels classified as signal, which will affect the computation of the centroid, and the execution time. Fig. 11 depicts the sequence of steps performed in the estimation of the centroid with the optimal selection of parameters.

From Fig. 11 we can see that the target, TOPEX/Poseidon, was deeply embedded in background noise. After the convolution with a median filter, the shape of the target was enhanced enabling a clear identification. After the background subtraction and masking of all

non-positive pixels, it can be seen that the background was effectively removed and that the centre of mass will indeed be estimated for the target.

5.2. Statistical and geometrical considerations

In Aperture Photometry we saw that placing rings around the source will approximate a PSF with a symmetrical shape. The estimation of the background depends on the type of estimator, the number of samples used for its estimation and the location of the samples within the frame. Since the background affects the estimation of the signal, after its subtraction, ideally the outer rings must be placed nearby the source. The likelihood of finding trails from stars, saturated pixels, or a partial area of the frame with a brighter background is rather high, therefore we chose an M-estimator, the median, which proves to have a bounded influence function [33]. A bounded influence function means that the estimator is more resilient to outliers if the latter is compared to a L-estimator, e.g. the arithmetic mean. Note that the same principle was taken into consideration for the selection of the autoregressive moving median in the active tracking approach showed in Section 4.

The implementation of apertures, i.e. circles, is more computationally expensive than using the circumscribed square of the circle. First, we compared the estimation of the background using the subframe against placing circular apertures. In the same comparison, we include the solutions using the median, with its respective median absolute deviation, and the mean, with its respective standard deviation (Top plot in Fig. 12). We can see how the mean is affected by the inhomogeneous background, larger standard deviation, when using the entire
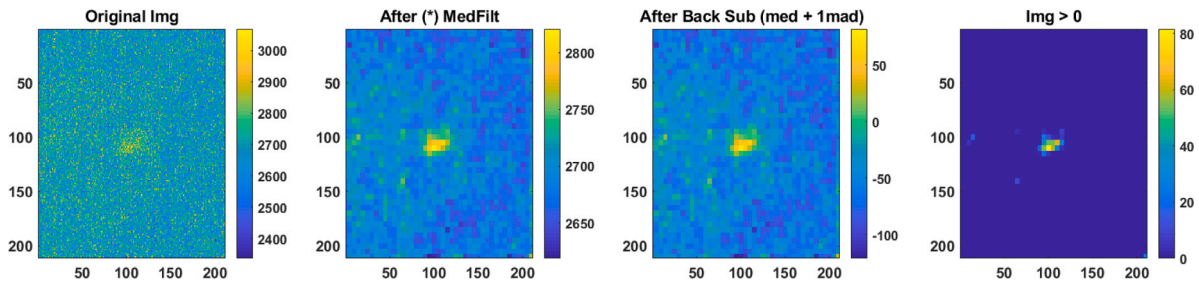
Fig. 11. Sequence of steps performed for the estimation of the centroid. The first image to the left shows a portion of the original frame. The second shows the result after convolving the subframe against a median filter using a kernel of 9×9 pixels and a step size of 5 pixels. The third shows the result after subtracting the estimated background. Finally, the last image shows all non-positive values masked to zero. Units colorbars: ADU. The X and Y axes correspond to the pixel position on the subframe.
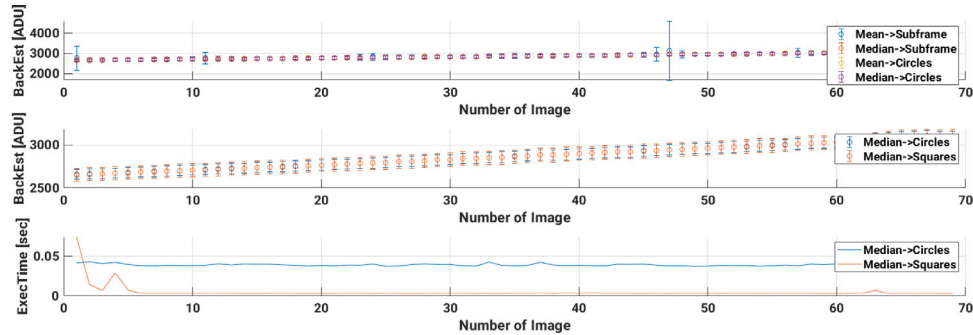

Fig. 12. Top: estimation of the background using the entire subframe vs. circular apertures using the mean, with its standard deviation, and the median with its median absolute deviation. Middle: estimation of the background with the median and its associated median absolute deviation using circles and squares. Bottom: execution time for the estimation of the background using circles and squares.

subframe for the estimation of the background. The use of the subframe or apertures with the median estimator does not show significant variations, as expected, due to the aforementioned properties of the estimator. The middle and bottom plots in Fig. 12 show the estimation of the background varying the geometry of the aperture from a circle to the circumscribed square of the circle, and the computational time, respectively. The gain in execution time using squares is noticeable while preserving the value of the estimated background, therefore we decided to implement it in the real-time system.

6. Results: Algorithm implementation

The current study focused on the conceptual basis of algorithms to implement the stare and chase observation strategy. In the previous section, we explored different possibilities for the object recognition and tracking phases highlighting the benefits of the selected choices. At this stage, we will review the steps that we have conducted in order to reach the implementation of the stare and chase observation strategy. After the study of the different methods available for object recognition, it was demonstrated that the aperture photometry was more resilient to the variabilities presented by the sky background and system constraints. Once angular observations are available, the chasing phase begins. The use of an immediate initial orbit determination showed that it does not always follow the object until it sets, within the same pass, if it is only estimated with the first few angular observations available from the staring mode. Furthermore, the inclusion of the updated ephemerides in highly automated systems may require the restart of a session which can lead to potential loose of a fast-moving target with a low culmination pass. As a consequence of the feasibility study, we decided to develop a closed-feedback loop combining object detection and tracking. Finally, we tested different tuning configurations to achieve the best performance in terms of computational running time. Next, we will analyse the implementation in a real case when the tracking camera is working in parallel to the
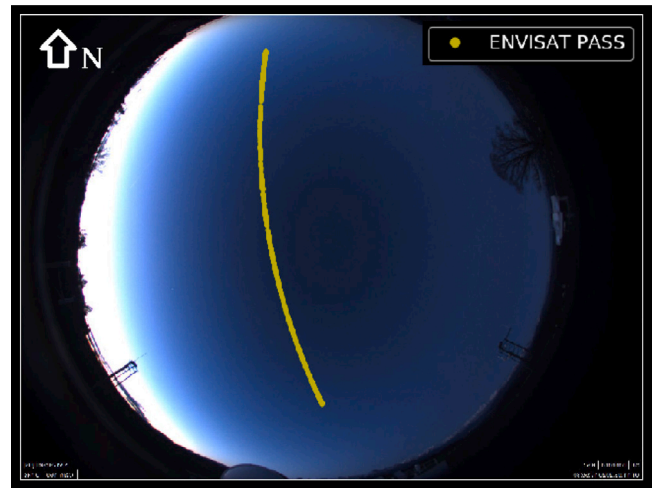

Fig. 13. ENVISAT pass over Zimmerwald on the 11th of March 2020 at 17:24 UTC.

SLR system. Fig. 13 depicts an all-sky image and the observed south–north pass over Zimmerwald for the decommissioned satellite ENVISAT observed on the 11th of March 2020 at 17:24 Coordinated Universal Time (UTC).

The selected pass had a high culmination (70°) near the terminator. In particular, the low elevation regions are still bright since the Sun was only a few degrees below the horizon. That situation presents a challenge to the stare and chase observation strategy, in particular for the object recognition phase, besides being a usual scenario for the observation of space debris.

Fig. 14 shows that from 17.42 to 17.44 h the estimation of the centroid from the object recognition and the prediction by the filter are in good agreement (differences smaller than ten pixels). Before 17.45 h we see
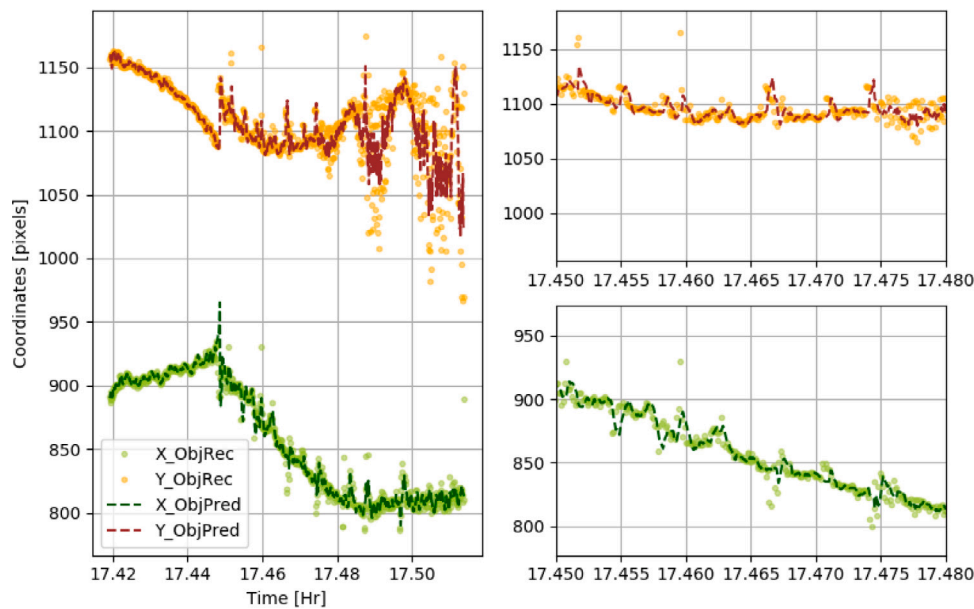
Fig. 14. Time series of the object image centroid after its estimation with the object recognition procedure and predicted values by active tracking for the decommissioned satellite ENVISAT on the 11th of March 2020. Left: complete pass. Right: detail in the Y (Top) and X (bottom) components. The results were acquired in real time.
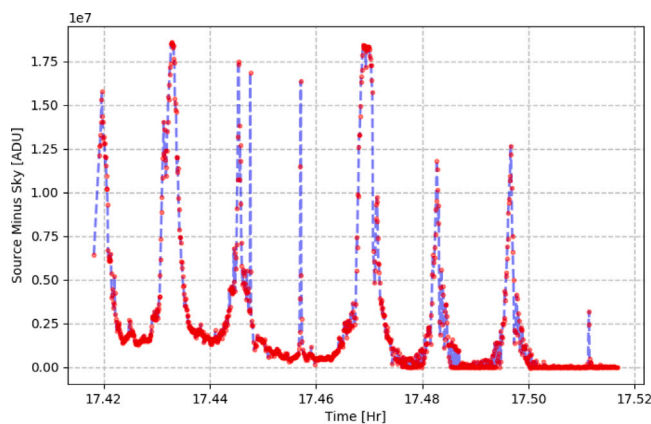

Fig. 15. Apparent brightness changes acquired in real time by the tracking camera for the decommissioned satellite ENVISAT on the 11th of March 2020.

a sudden change in the trajectory of the target, neglected by the filter at the beginning, since at deviating from the median of the error window the measurements were marked as outliers. Once the filter desaturated, it was able to continue the tracking. In the right plots shown in Fig. 14, we can see how resilient the filter is in terms of neglecting wrong measurements coming from the object detection. The reason for those wrong measurements is that the contrast of the brightness between source and background is rather low. That means that after we subtract the background, there are scattered pixels through the subframe which do not belong to the target thus affecting the estimation of the centroid.

The filter is able to smooth enough the trajectory so that we can retrieve the real-time light curve of the target showing noticeable periodicities as depicted in Fig. 15.

Besides being able to track the target and generate real-time information about its attitude, the main goal was to keep the target within the field of view of the laser beam for maximizing chances of retrieving ranges. In Fig. 16, we can see the detections by our SLR real-time filter. From the observed pass, we were able to retrieve 2708 hits for an 8 min pass using a repetition rate of 100 Hz (black dots in Fig. 16), a number which can be improved in a post-processing step as many returns were

not detected by the SLR real-time filter (string of grey dots). The along-track error for this case was estimated to be −0.007 s. The range gate was initially set to 600 nanoseconds, shrinking to 40 nanoseconds as soon as the SLR real-time filter detected hits.

Since March 2020 until today, we have been using the automated mode of the tracking camera regularly. The only drawback of the current implementation is that the corrections sent by the tracking camera must be integrated into the Proportional–Integral–Derivative (PID) control algorithm running within our telescope controller. At a frequency higher than 0.5 Hz, the corrections are buffered leading to an undesired drifting effect. Nevertheless, the current implementation has proved to keep the target within the subframe even if the error in the a priori orbit was half of the field of view of the tracking camera, being that a worst-case scenario.

7. Summary and outlook

The stare and chase is the resulting observation strategy after the merge of two well-known observation strategies namely survey and follow-up. The main aim was to use a passive-optical system to correct the pointing of the telescope locking the target within the field of view of the laser beam. The use of laser ranges will improve drastically the orbit determination of the target facilitating its future reacquisition. In particular, through the presented research we were able to:

- **Validate the measurements acquired by the tracking camera mounted on ZIMLAT.** The validation included an improvement in the measurement accuracy. The improvement of the accuracy was done by requesting the timestamp from the telescope PMAC. In addition, the modelling of the laser beam position in the camera reference system, through a 2D Fourier expansion, proved to contribute significantly to the improvements in accuracy. The validation of the measurements was done via an orbit determination scheme and by using precise ephemerides in form of CPF. Hence, proving that the pointing of the telescope can be used to define the orientation of the camera reference system without reference stars. The latter would not be feasible in case of fast moving SLR targets or in case of daylight observations, as not enough reference stars would be recorded by the camera.
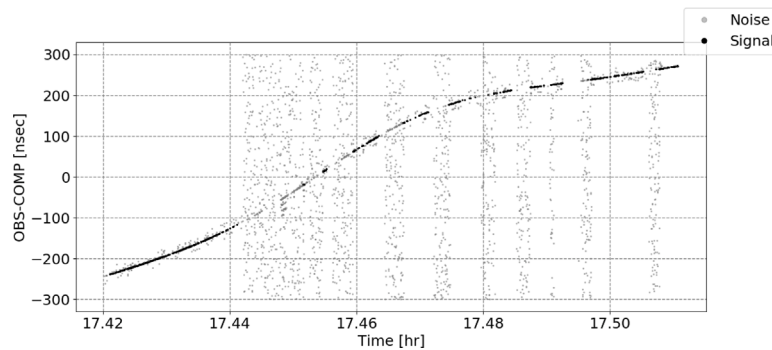
Fig. 16. Real time detections by our SLR system for the decommissioned satellite ENVISAT on the 11th of March 2020.

- **Compare and implement three object recognition algorithms for the staring phase.** Those methods are the fitting of a defined PSF, the template matching and the aperture photometry. The fitting of a PSF takes on average 5 s which is above the limit for a real-time application; it also needs of a priori knowledge of the object image and its characteristics, and it is sensitive to trails of stars. The same sensitivity, with respect to the background, applies to the template matching approach. The aperture photometry method proved to be more resilient after proper selection of tuning parameters such as the kernel and step size used by the median filter.
- **Compare and implement two possibilities for the chasing phase.** Those are the use of an initial orbit determination and active tracking. The use of an initial orbit determination approach might not be optimal for highly automated systems, since the inclusion of the newly generated ephemerides may not be done within an existing session. In such cases, a real-time correction for the pointing of the telescope is preferred. In combination with the object recognition algorithm, we implemented a filter used for predicting the coordinates of the target using a sliding window approach. The trajectory of the target is modelled as a polynomial preferably with a degree lower than three. The number of data points within the sliding window may vary depending on the exposure time, but a number of nine historical records demonstrated to be enough to keep the target centred within the field of view of the laser beam. Additional windows for error control and outlier detection run in parallel to the one used for the trajectory to ensure robustness.
- **Optimize the selected algorithms for its implementation in a real-time system.** We studied suitable parametrizations that will allow for a reduction in the computational time while complying with the stringent requirements of our system namely: the field of view of the laser beam. The most expensive computational operations are within the object recognition phase, specifically the convolution of the subframe against the median filter, and the estimation of the background. However, the time taken for the estimation of the background was reduced by changing the geometrical pattern to squares from circles.
- **Increase the set of observables to azimuth, elevation, range and apparent brightness.** The outstanding by-product of the object recognition phase is a real-time light curve depicting apparent changes in brightness of the object with respect to time, which can be used for orbit improvement and attitude determination of RSO. All the gathered information within our 4-dimensional measurement set was validated and is ready for conducting more case studies than the one provided in Section 6. Finally, we showed that the observations of a longer arc, besides the fusion of observables of a different type, will allow the reacquisition of the object for subsequent passes.

Soon, we are planning to implement the estimation of the coordinates of the laser beam on the camera reference system automatically. By doing so, each single observation night can be used to collect the information needed to estimate the laser beam on the camera reference system (see Section 2.2), without a special session storing and post-processing images, increasing the amount of data and data distribution over the sky. Moreover, the corrections to the predicted trajectory should be computed as along-track/cross-track components. The latter showed a smoother behaviour over time when compared with corrections in azimuth and elevation as in Fig. 9. Finally, for complete automation of the tracking camera, we are planning to implement an autofocus function. Currently, the focus must be iteratively adjusted by the operator.

Declaration of competing interest

The authors declare that they have no known competing financial interests or personal relationships that could have appeared to influence the work reported in this paper.

Acknowledgements

The first author would like to express his gratitude to the Swiss National Science Foundation for providing the funds that supported the current study. Furthermore, he would like to explicitly thank Dr. Peter Schlatter for developing and implementing the baseline of the tracking camera software and for all discussions.

References

[1] M.R. Pearlman, J.J. Degnan, J.M. Bosworth, The international laser ranging service, Adv. Space Res. (2002) http://dx.doi.org/10.1016/S0273-1177(02)00277-6.
[2] D. Gibson, E. Pearce, M. Blythe, P. Trujillo, Orbital debris characterization: ETS staring survey [1951-02], Astron. Astrophys. Berlin 1 (1951) (1993) 11.
[3] B. Greene, Y. Gao, C. Moore, Laser tracking of space debris, Tech. Rep., 2002.
[4] C.H. Smith, The EOS space debris tracking system the EOS space debris tacking system and RazorView demonstration, in: AMOS Conference, no. December 2002, 2006, pp. 799–807.
[5] K.J. Abercromby, P. Seitzer, H.M. Rodriguez, E.S. Barker, M.J. Matney, Survey and chase: A new method of observations for the Michigan Orbital DEbris Survey Telescope (MODEST), Acta Astronaut. 65 (1–2) (2009) 103–111, http://dx.doi.org/10.1016/j.actaastro.2009.01.031.
[6] T. Hasenohr, D. Hampf, P. Wagner, F. Sproll, J. Rodmann, L. Humbert, A. Herkommer, W. Riede, Initial detection of low earth orbit objects through passive wide angle imaging systems, in: Deutscher Luft- Und Raumfahrtkongress 2016, 2016, pp. 1–7.
[7] M.A. Steindorfer, G. Kirchner, F. Koidl, P. Wang, A. Antón, J. Fernández Sánchez, K. Merz, Stare and chase of space debris targets using real-time derived pointing data, Adv. Space Res. (2017) http://dx.doi.org/10.1016/j.asr.2017.06.026.
[8] D.A. Marsillach, S. Virani, M.J. Holzinger, Real-time hardware-in-the-loop hand-off from a finder scope to a larger telescope, in: 1st IAA Conference on Space Situational Awareness (ICSSA) Orlando, FL, USA IAA-ICSSA-17-0X-XX, Vol. 0X, No. 1, 2017, pp.1-18.

[9] Andor Neo 5.5 sCMOS Specifications, Andor - Oxford Instruments, 2021, [Online]. Available: https://andor.oxinst.com/assets/uploads/products/andor/documents/andor-neo-scmos-specifications.pdf. (Last Accessed 17 January 2021).

[10] E. Cordelli, J. Rodriguez-Villamizar, P. Schlatter, P. Lauber, Real time improvement of orbits of space debris by fusing SLR and astrometric data acquired by a night-tracking camera, in: 21st International Workshop on Laser Ranging, 2018.

[11] J.J. Condon, Gbt Pointing Equations, Tech. Rep. Memo Series, NRAO, 1992.

[12] M. Pearlman, D. Arnold, M. Davis, F. Barlier, R. Biancale, V. Vasiliev, I. Ciufolini, A. Paolozzi, E.C. Pavlis, K. Sośnica, et al., Laser geodetic satellites: a high-accuracy scientific tool, J. Geod. 93 (11) (2019) 2181–2194, http://dx.doi.org/10.1007/s00190-019-01228-y.

[13] B.D. Tapley, B.E. Schutz, G.H. Born, Statistical Orbit Determination, ISBN: 9780080541730, 2004.

[14] Space-track, 2020, [Online]. Available: https://www.space-track.org/auth/login. (Accessed 5 October 2020).

[15] S.B. Howell, Two-dimensional aperture photometry - Signal-to-noise ratio of point-source observations and optimal data-extraction techniques, Publ. Astron. Soc. Pac. (1989) http://dx.doi.org/10.1086/132477.

[16] M. Born, E. Wolf, Principles of Optics: Electromagnetic Theory of Propagation, Interference and Diffraction of Light, Elsevier, 1999.

[17] E. Cuevas, V. Osuna, D. Oliva, Template matching, Stud. Comput. Intell. (2017) http://dx.doi.org/10.1007/978-3-319-51109-2-4.

[18] M. Masias, J. Freixenet, X. Lladó, M. Peracaula, A review of source detection approaches in astronomical images, Mon. Not. R. Astron. Soc. (2012) http://dx.doi.org/10.1111/j.1365-2966.2012.20742.x.

[19] S. Thomas, T. Fusco, A. Tokovinin, M. Nicolle, V. Michau, G. Rousset, Comparison of centroid computation algorithms in a Shack-Hartmann sensor, Mon. Not. R. Astron. Soc. (2006) http://dx.doi.org/10.1111/j.1365-2966.2006.10661.x.

[20] M.E. Everett, S.B. Howell, A technique for ultrahigh-precision CCD photometry, Publ. Astron. Soc. Pac. (2001) http://dx.doi.org/10.1086/323387.

[21] J.J. Moré, The Levenberg-Marquardt algorithm: Implementation and theory, 1978, http://dx.doi.org/10.1007/bfb0067700.

[22] S.W. Smith, The Scientist and Engineer's Guide to Digital Signal Processing, California Technical Publishing, USA, ISBN: 0966017633, 1997.

[23] F.R. Chromey, To Measure the Sky: An Introduction to Observational Astronomy, Cambridge University Press, ISBN: 978-0-511-72954-6, 2010.

[24] K.A. Collins, J.F. Kielkopf, K.G. Stassun, F.V. Hessman, Astroimagej: Image processing and photometric extraction for ultra-precise astronomical light curves, Astron. J. 153 (2) (2017) 77, http://dx.doi.org/10.3847/1538-3881/153/2/77.

[25] G. Beutler, Methods of Celestial Mechanics Volume I: Physical, Mathematical, and Numerical Principles, 1st ed., in: Astronomy and Astrophysics Library, Springer Berlin Heidelberg, Berlin, Heidelberg, ISBN: 3-642-10529-7, 2005.

[26] G. Groenewegen, A. van Rooij, The stone-weierstrass theorem, in: Spaces of Continuous Functions, Atlantis Press, Paris, ISBN: 978-94-6239-201-4, 2016, pp. 22–28, http://dx.doi.org/10.2991/978-94-6239-201-4_3.

[27] G.E. Box, G.M. Jenkins, G.C. Reinsel, Time Series Analysis: Forecasting and Control, John Wiley & Sons, 2011.

[28] S.K. Sengupta, S.M. Kay, Fundamentals of statistical signal processing: Estimation theory, Technometrics (1995) http://dx.doi.org/10.2307/1269750.

[29] P.J. Rousseeuw, C. Croux, Alternatives to the median absolute deviation, J. Amer. Statist. Assoc. (1993) http://dx.doi.org/10.1080/01621459.1993.10476408.

[30] R.B. Schnabel, E. Eskow, A revised modified Cholesky factorization algorithm, SIAM J. Optim. (1999) http://dx.doi.org/10.1137/S105262349833266X.

[31] MATLAB 9.6.0.1072779 (2019a), The Mathworks, Inc., Natick, Massachusetts, 2019.

[32] Delphi XE2 datasheet, 2021, https://edn.embarcadero.com/article/images/41559/Delphi_XE2_datasheet.pdf. (Last Accessed 17 January 2021).

[33] J. Rodriguez-Villamizar, Dynamical Compensation Methods in Uncertain Systems Applied to Orbit Determination (M.Sc. thesis), Technische Universität München, 2017, p. 200, Masterarbeit, https://mediatum.ub.tum.de/node?id=1429937.